Available online at www.sciencedirect.com
ScienceDirect
Medical Image Analysis 11 (2007) 62–78
MEDICAL IMAGE ANALYSIS
www.elsevier.com/locate/media

A biplanar fluoroscopic approach for the measurement, modeling, and simulation of needle and soft-tissue interaction

James T. Hing [a], Ari D. Brooks [b], Jaydev P. Desai [c,*]

[a] Program for Robotics, Intelligent Sensing, and Mechatronics (PRISM) Laboratory, Drexel University, Philadelphia, PA 19104, United States
[b] Drexel University College of Medicine, Philadelphia, PA 19104, United States
[c] Department of Mechanical Engineering, University of Maryland, College Park, MD 20742, United States

Received 1 October 2005; received in revised form 25 September 2006; accepted 28 September 2006
Available online 17 November 2006

Abstract

A methodology for modeling the needle and soft-tissue interaction during needle insertion is presented. The approach consists of the measurement of needle and tissue motion using a dual C-arm fluoroscopy system. Our dual C-arm fluoroscopy setup allows real time 3-D extraction of the displacement of implanted fiducials in the soft tissue during needle insertion to obtain the necessary parameters for accurate modeling of needle and soft-tissue interactions. The needle and implanted markers in the tissue are tracked during the insertion and withdrawal of the needle at speeds of 1.016 mm/s, 12.7 mm/s and 25.4 mm/s. Both image and force data are utilized to determine important parameters such as the approximate cutting force, puncture force, the local effective modulus (LEM) during puncture, and the relaxation of tissue. We have also validated the LEM computed from our finite element model with arbitrary needle puncture tasks. Based on these measurements, we developed a model for needle insertion and withdrawal that can be used to generate a 1-DOF force versus position profile that can be experienced by a user operating a haptic device. This profile was implemented on a 7-DOf haptic device designed in our laboratory.

Keywords: Surgical simulation; Soft-tissue modeling; Needle insertion simulation; Local effective modulus; Haptic feedback

1. Introduction

There are multiple procedures in surgery, where accurate placement of needles is vital to the success of the procedure. One such procedure is prostate brachytherapy during which the surgeon inserts a needle through the perineum, fatty tissue, muscle and then prostate to place radioactive seeds. The goal for seed placement is to maximize the radiation dose to the tumor while minimizing radiation doses to the surrounding tissue such as the rectum, bladder and urethra. Accurate seed positioning inside the prostate is very important for the success of the procedure. Minor deviations in seed placement caused by gland and tissue compression and needle retraction, gland edema, and needle deflections, can lead to significant areas of over dosage or under dosage to the gland (Vicini et al., 1999). For various needle insertion procedures such as prostate brachytherapy, lumbar puncture and liver biopsy the success rate of the procedure is directly related to the clinician's level of expertise. Therefore, improvement in the complication rates will be dependent on improving the training tools used by clinicians. Obtaining real world parameters for characterizing needle and soft-tissue interaction is the first step towards developing a model to provide accurate haptic feedback in a training simulator for needle insertion tasks.

To date, a number of researchers have explored techniques to improve surgeons' skills in procedures where little haptic and visual feedback exists. These mainly take the form of haptic simulators, for procedures such as catheter insertion (Gobbetti, 2000), lumbar puncture (Gorman, 2000), epidural blocks (Hiemenz, 1996; Brett et al., 2000),

* Corresponding author. Tel.: +1 301 405 4427; fax: +1 301 314 9477.
E-mail addresses: jth23@coe.drexel.edu (J.T. Hing), Ari.Brooks@DrexelMed.edu (A.D. Brooks), jaydev@umd.edu (J.P. Desai).

1361-8415/$ - see front matter © 2006 Elsevier B.V. All rights reserved.
doi:10.1016/j.media.2006.09.005

endoscopic surgeries, and laparoscopic surgeries. From the surgical simulation viewpoint, most tissue interaction models assume mechanical properties and develop methods to efficiently solve the tissue simulation problem for robot-assisted surgery/training. Several simulators have developed very sophisticated virtual environments that allow for plastic deformations of the material and interactions in multiple dimensions (Picinbono et al., 2001; Forest et al., 2002). However, it has been difficult to populate these models with data from real tissues.

"Global" elastic deformations of real and phantom tissues have been studied extensively in previous work through simple poking interactions (d'Aulignac et al., 2000; Brouwer, 2001; Ottensmeyer and Salisbury, 2001; Kennedy et al., 2002; Kennedy et al., 2002). However, these methods are simplistic since they do not consider the complex boundary conditions that are normally present, both internal to the organ and on the exterior surface. For needle insertion tasks, simulation and modeling have been conducted by a number of researchers (Stoianovici et al., 1998; Brett et al., 2000; Smith et al., 2001; DiMaio and Salcudean, 2002; Kataoka et al., 2002; Simone, 2002; Alterovitz et al., 2003; Nienhuys and van der Stappen, 2003; Hong et al., 2004; Magill et al., 2004. Only a few groups have modeled and studied the measurement of forces during needle insertion into soft tissue and the effects of needle geometry on the deflection during needle insertions into homogeneous material (Brett et al., 2000; Kataoka et al., 2002; Simone, 2002; O'Leary et al., 2003; Heverly et al., 2005). In this paper, we offer a different approach to separating the different forces acting on the needle and obtaining the cutting force. Our method requires only one force sensor and we can internally image soft tissue movement during a needle insertion and withdrawal task. Needle deflection is also an important part of our study because it has been observed during surgical procedures such as prostate brachytherapy that the needle can deflect from the initial insertion point as it is being inserted through the body by more than 10 mm (Cormack et al., 2000).

Simulations based on real needle insertion forces into soft tissues have been conducted by Brett et al. (2000); Simone (2002); Heverly et al. (2005)). In the work of Heverly and Simone (Simone, 2002; Heverly et al., 2005), the simulation is only a visual reproduction of the forces during needle insertion. In Brett et al. (2000), a force feedback device is integrated into the simulator but the simulation is only for needle insertion and does not include needle withdrawal. In this paper, we produce a simulation of needle insertion and withdrawal with haptic feedback using the 7 degree of freedom haptic feedback device developed in our laboratory. The simulated forces are based on ex vivo experimental data from needle insertion and withdrawal in a soft tissue specimen.

Imaging modalities used during needle insertion into soft tissue have mainly been utilized for needle guidance. However, some researchers have used the imaging modalities to track fiducials during needle insertion into clear homogeneous phantom tissues to obtain properties about the needle and phantom tissue interactions (DiMaio and Salcudean, 2002; Crouch et al., 2005). However, these experiments required knowledge of the properties of the phantom tissues prior to experiments and also required the phantom to have homogenous material properties. Kerdok et al. (2003) developed the truth cube which consists of fiducials implanted inside a homogeneous phantom tissue. The 3D motion of the markers during compression of the phantom was used to validate a finite element model. This work was one of the first approaches to quantify the internal local tissue movement. However, it did not include needle insertion nor was it conducted on biological tissues. Our approach involves tracking fiducials using two C-arm fluoroscopes. The fiducials are placed "semi-randomly" in a soft tissue. With the data collected from our experimental setup, we can extract the necessary parameters such as puncture force, cutting forces, and local effective modulus, required for accurate modeling of needle and soft-tissue interaction. We were also able to validate the finite element model for needle insertion into soft tissue for an arbitrary needle insertion task. To our knowledge, there has been no prior work on measuring in real-time the 3-D movement of fiducials (beads) in soft tissue during needle insertion and we believe that our approach using two C-arms is novel. This type of reality based modeling is critical for providing accurate haptic feedback in surgical simulation. Fig. 1 shows a schematic of the proposed reality based modeling approach.

This paper is divided into five sections. In Section 2, we discuss the materials and methods used for tracking the needle and implanted markers in the soft tissue during an insertion and withdrawal task. We also introduce our 3D finite element model and the 7 degree-of-freedom (DOF) haptic device used for simulation. The results are shown in Section 3, which also includes the results from the needle insertion simulation. Section 4 is our discussion of the results and in Section 5 we present our conclusions.

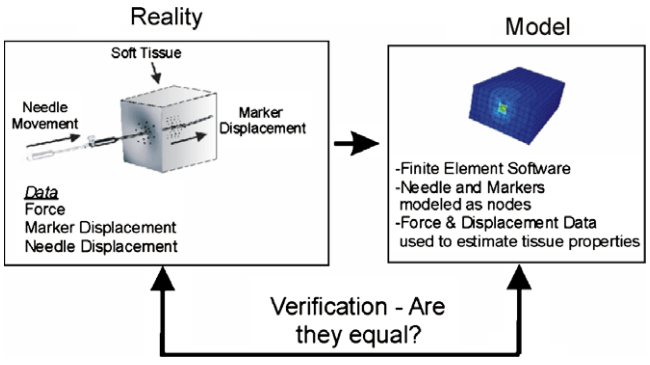

Fig. 1. Schematic of the proposed reality-based modeling approach for accurate needle and soft-tissue interaction in a training simulator for prostate brachytherapy. The reality side (left) shows the data collected such as force, marker displacement and needle displacement. The model side (right) shows a finite element model and lists the inputs used to develop the model.

2. Materials and methods

Table 1 demonstrates our proposed approach for modeling needle and soft-tissue interaction during a needle insertion and withdrawal task. This paper presents the following: (a) the computational model for needle puncture to estimate the local tissue stiffness prior to puncture and (b) reality-based estimation of the friction force during needle insertion and withdrawal, and (c) the quantification of the force versus displacement plot during tissue relaxation.

2.1. Experimental apparatus and data acquisition

2.1.1. Dual C-arm fluoroscopes for fiducial tracking

Fig. 2 shows the dual C-arm experimental setup for tracking the motion of beads inside the soft tissue. To view the internal tissue movement during needle insertion and withdrawal, forty 1 mm diameter stainless steel beads were inserted into the soft tissue. These beads were chosen because of their radiopacity (ability to block X-ray transmission) and their size, which was small enough to not affect the properties of the soft tissue or impede the needle insertion path. Validation of this is shown in the results Section 3.1.1, where we compared the needle insertion forces and tissue deformation during puncture with and without beads. As an initial approach, we are using 40 beads to measure the internal movement of the tissue. The beads were placed in a grid pattern spaced approximately 10 mm apart from one another and in such a way to minimize occlusion between beads during imaging. In general, the orientation of the tissue can also be changed to minimize occlusion in C-arm experiments. Each bead was inserted one at a time perpendicular to the experiment needle path using an 18 gauge needle to an approximate depth of 10–20 mm from the tissue surface. Fig. 3 shows the X-ray image of both the top and side view of the tissue. The OEC 7700 (side view) and OEC 9600 fluoroscopes (top view) were used to image the needle and implanted markers inside of the tissue during experiments. The OEC 9600 by OEC Medical Systems Inc. has a 12 in. tri-mode image intensifier with 44 lp/cm central resolution and 42 lp/cm peripheral resolution at 70% radius. The OEC 7700 by OEC Medical Systems Inc. has a 9 in. tri-mode image intensifier.

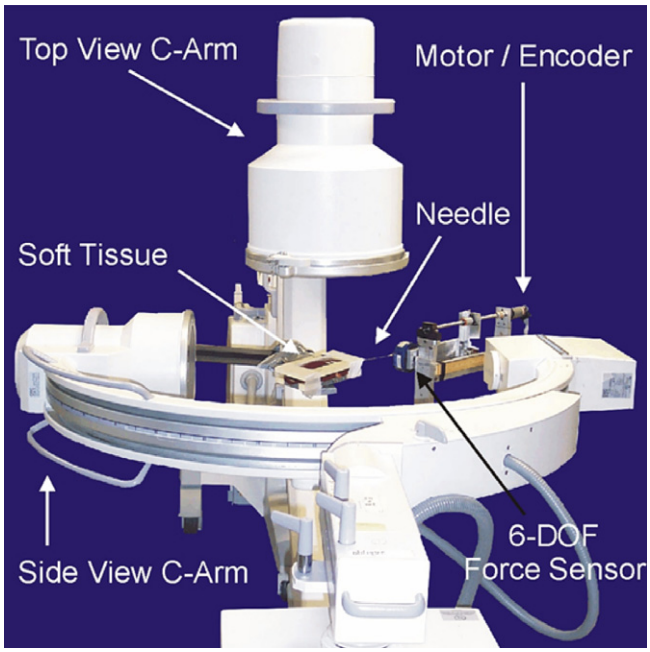

Fig. 2. Dual C-arm fluoroscope setup. OEC 9600 fluoroscope is imaging the top view and the OEC 7700 fluoroscope is imaging the side view. The soft tissue sample is located in the center of the two C-arms.

Table 1
Modelling needle and soft-tissue interaction during needle insertion and withdrawal

Tasks	Data Acquired
1. Needle Puncture 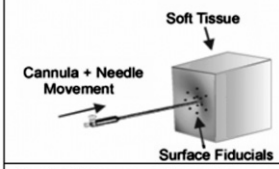	-Fiducial movement on skin surface -Force vs. displacement prior to skin puncture
2. Soft-tissue and needle interaction (needle insertion + needle withdrawal) 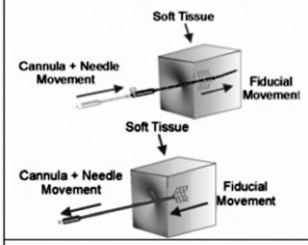	-Force vs. displacement -Fiducial movement -Local tissue motion -Global tissue movement
3. Tissue relaxation 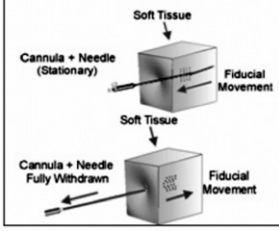	-Force decay over time (after insertion) -Fiducial movement -Local tissue movement -Global tissue movement

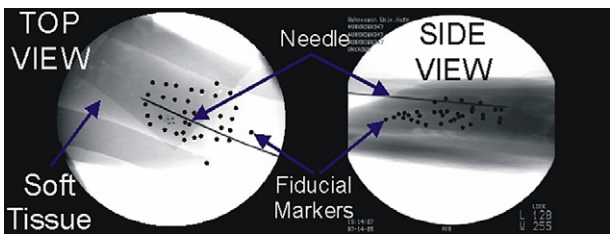

Fig. 3. Images acquired from both C-arms during needle insertion. The markers have been enhanced for clarity. Each image is the raw image obtained from the fluoroscope before post processing distortion correction. The left image is the top view and the right image is the side view.

C-arm fluoroscopy allows for real time X-ray imaging, where X-rays are generated at the transmitter (source) and photographed at the receiver (detector). The C-arm's were positioned so that their imaging planes were orthogonal to each other, allowing for real time imaging of the side and top views of the implanted markers and needle tip during insertion. Each C-arm has a graduation mark indicating the angle of rotation and this was also verified using a level. The video from each C-arm was captured onto a hard disk using a video capture device (Pinnacle Systems – Dazzle Digital Video Creator 150) at 30 fps and at a resolution of 720×480 pixels. We performed the calibration of the distortion and magnification correction in the C-arm images and this procedure is described in more detail in Appendix.

2.1.2. Needle insertion device and tissue constraint

The needle apparatus was designed to measure the forces on a surgical needle during insertion into soft tissue. Fig. 4 is a close up view of the needle insertion device and tissue constraint. A proportional derivative controller was used to achieve constant velocities of 1.016 mm/s, 12.7 mm/s and 25.4 mm/s of the needle during insertion and withdrawal. The needle insertion device consists of a geared DC motor, an incremental encoder and a 6 axis force/torque sensor (JR3) with 0.278 N accuracy and ± 14 bit resolution. The needles used for the experiments were 18-gauge prostate seeding needles (Mick Radio Nuclear Instruments, Inc.) of 20 cm length as shown in Fig. 5. The needle is a typical prostate seeding needle with a symmetric needle tip.

Porcine liver was used as our soft tissue specimen. We chose porcine liver because it is easy to obtain and offers a large workspace for quantifying needle and soft-tissue interactions. While the numerical results presented in this paper are specific to that of the liver, the methods proposed

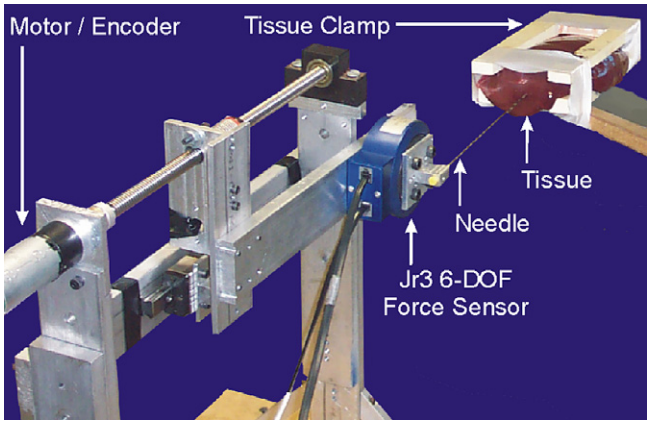

Fig. 4. Close-up of the needle insertion apparatus. The needle is an 18 gauge, 20 cm long prostate seeding needle and is inserted into the tissue at a constant velocity while the JR3 force sensor collects the force data. The tissue clamp is in place to secure the soft tissue to the radio-opaque table during needle insertion and withdrawal.

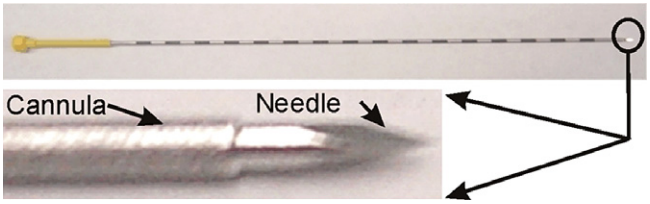

Fig. 5. Various components of a typical after loading prostate brachytherapy seeding needle. The needle also known as the trocar, is surrounded by a hollow tube known as a cannula. The needle and cannula together make up the "needle" referred to in this paper.

are applicable to a variety of percutaneous procedures. Beads were placed inside the tissue approximately 2 h after it was excised from the pig. During the 2 h between the removal of the liver and the insertion of the beads, the liver remained in a saline solution to retain materials properties as close to the original unperfused excised state as possible. After bead insertion, the liver was immediately frozen until just before the experiments when it was allowed to thaw completely before use. This preserves the liver properties as close as possible to its initial excised state (Davies et al., 2002). Three liver specimens were used and each specimen underwent five needle insertions at constant speeds, namely: 1.016 mm/s, 12.7 mm/s and 25.4 mm/s.

The tissue samples were placed onto a flat plate and clamped such that the sides and back of the tissue were constrained from movement, leaving the front of the tissue free to move and unobstructed for needle insertion. To keep the setup as radiolucent (permits the penetration and passage of X-rays) as possible, the plate and clamp were made from machineable plastic and the clamp was held secure onto the tissue using surgical tape as seen in Fig. 4. There is no device to help guide the needle into the tissue as it would introduce extraneous reaction forces which would make it impossible to ascertain the true tissue and needle interaction forces.

2.1.3. Marker registration

Correlation of each marker in the top view image with its location in the side view image is obtained by rotating one C-arm from 0 to 90° while continually capturing the X-ray images during the rotation. Each marker was tracked as it moved in the image during the rotation. This was done before inserting the needle for each soft tissue sample.

After marker registration, the needle was moved into place. The distance of the livers sample with respect to the C-arm detectors was obtained by imaging radio-opaque rulers placed on the liver sample in both the top and side view images. For synchronization of the top and side view images, a radio-opaque object is imaged in both X-ray fields and immediately removed at the start of insertion (start of force and position capture as well). The needle is then inserted approximately 90 mm into the soft tissue at insertion speeds of 1.016 mm/s, 12.7 mm/s and 25.4 mm/s. During needle insertion, the force sensor captured the forces

acting on the needle at 1000 Hz while the side and top view C-arms continually recorded X-ray images of the needle position and the movement of the markers inside the tissue. After each insertion, the needle was moved to a different position in the soft tissue to minimize the chance of following a previous insertion path.

The centriods of the markers and needle tip were extracted from the top and side view images using MATLAB image processing toolbox. The trajectories were reconstructed by applying the appropriate calibration corrections and kinematic transformations. The videos from the C-arms for each insertion were loaded separately into MATLAB as (.avi) files. An image difference algorithm was then applied using an image of the soft tissue with no beads to the frame being analyzed. This eliminated the outside boundaries of the images and highlighted only the marker and needle movement between the frames.

2.1.4. C-arm tracking accuracy

The accuracy of the measurements of the bead movement and needle deflection rely on the ability of our tracking algorithm to account for the distortions and magnifications inherent in the C-arm images. We tested the ability to accurately track the movement of both the beads and the needle in 3D using the dual C-arm setup by extracting the displacement of the needle tip in the C-arm images and comparing it with the needle displacement data obtained from the screw motion (motor rotation is captured by the encoder which allows us to compute the translational motion of the needle). The motor encoder presents the magnitude displacement of the needle tip during the insertion.

2.2. Needle deflection and marker movement

In our studies, we measured the full insertion deflection of the needle tip from its straight line trajectory for each needle insertion trial. We also measured the implanted bead displacements which represented the local tissue movement during each needle insertion and withdrawal. The movement of the beads was used to evaluate different needle and tissue interaction properties and validate our finite element models.

2.3. Soft-tissue property estimation

Needle insertion consists of four events: initial puncture, insertion, relaxation and withdrawal. We utilize the force information from each event to extract important information about the individual forces acting on the needle.

2.3.1. Separation of forces

Just before the needle has entered into the tissue and as the needle is inserted further into the soft tissue, it undergoes a series of macro and micro punctures where the force rises and drops. Areas of significant changes in stiffness or obstacles inside the tissue or tissue boundaries in a system of multiple soft tissues result in major puncture events where the tissue is deformed at the same rate as the velocity of the needle tip until cutting occurs. Typically, this leads to a steep rise in force followed by a sudden drop in force, signifying a puncture event. Outside of these puncture events, the force increases relatively linearly during insertion due to the increase in friction as the surface area of the needle inside the tissue increases. The instant tissue puncture occurs was estimated by the following approach. A marker placed close to the needle insertion point will move at the same velocity as the needle tip until puncture occurs. The time at which the relative velocity of the marker with respect to the needle tip is no longer zero, can be taken as the time of puncture. In our experiments with the C-arms, the relative velocities of the markers close to the needle insertion site are tracked along with the needle tip. Fig. 3 shows a tissue sample with markers located close to the needle tip. Since the needle consists of an inner needle and a cannula (see Fig. 5), there are two puncture events of the tissue which occur on the surface. The first puncture occurs when the needle tip penetrates the surface of the tissue and the second puncture occurs when the cannula punctures through the surface. The second puncture, i.e. the second time the markers move with the same velocity as the needle, is used in this study as the significant parameter because it is after the second puncture that the needle can be considered completely inserted into the tissue. Various internal puncture events can be identified by following the marker movement as the needle progresses inside the tissue. When local markers around the needle move with the same velocity as the needle tip (i.e. zero relative velocity between the needle tip and the marker), we can conclude that the needle is no longer cutting the tissue but is instead compressing it until puncture occurs.

To identify the start of kinetic friction on the needle, we adopted a similar approach. During the start of withdrawal of the needle, the needle does not slide inside the tissue but pulls the tissue in the direction of withdrawal until a threshold force to overcome the static friction and clamping force on the needle is overcome. After this point, the needle begins to slide inside the tissue and kinetic friction begins. Estimating the start of kinetic friction requires finding the point during withdrawal at which the relative velocity of the tissue with respect to the needle is no longer zero (corresponding to the moment when the needle is no longer dragging the tissue, but is instead sliding past it). During needle withdrawal, the needle is no longer cutting the tissue and hence, the only force acting on the needle (as measured by the force sensor) can be approximated to be the force of kinetic friction. Also during needle withdrawal, the needle does not start sliding within the tissue until the maximum slip force is reached. This hypothesis was verified by image analysis.

We also focused on quantifying the cutting force (the force required to cut tissue at the needle tip) during needle insertion into soft tissue, and obtaining the local effective

modulus of the tissue during the initial needle puncture of the tissue surface. Each of these values is important towards accurate simulation of a complete needle insertion and withdrawal task. Friction and cutting are major forces acting in the direction of insertion; therefore, the cutting force can be approximated by subtracting the force of friction from the total insertion force (Simone, 2002). In Simone et al., they obtained the friction coefficients for their Karnopp friction model by inserting a needle completely through a piece of soft tissue of known thickness and oscillating the needle. Our approach is different from Simone et al. because we used the friction force during withdrawal of the needle from the tissue and subtracted it from the total insertion force. We assumed that the lubrication of the shaft of the needle is the same for both needle insertion and withdrawal phases. During needle insertion we assume (based on observations) that the instant the needle cuts the tissue; the channel is immediately lubricated by blood. Also we assume that the local stress concentration at the tip of the needle caused by the cutting force has a minimal effect on the far field clamping force on the needle shaft.

2.3.2. Tissue relaxation

Tissue relaxation is an important parameter to understand when simulating seed placement for prostate brachytherapy since it provides information on surrounding seed movement (most importantly those close to the needle) after the needle comes to rest in the tissue or after the needle is withdrawn. In prostate brachytherapy, relaxation can cause a radioactive seed to be placed in an inaccurate location. Tissue relaxation can be observed by analyzing the force data as the needle is held in its full insertion position as well as by analyzing the internal tissue movement. Both the needle insertion and withdrawal phase contribute to tissue relaxation, namely relaxation of the tissue after the needle is fully inserted in the tissue and relaxation after the needle is completely withdrawn from the tissue.

Based on our experimental data, we can model the force representing the tissue relaxation process at the end of an insertion task as an exponentially decaying curve of the form:

$$y = a * \exp(-b * t) + c \quad (1)$$

where y is the force value in Newtons, t is the time in seconds and a, b, and c are constants. In our experiments, c represented the approximate steady-state force (ideally c would be the constant force when $t \to \infty$. b represented approximately how fast the force decayed from its starting force value to its decayed value, and a represented approximately how much the force changed from the start of the relaxation process ($t = 0$) to the end of the relaxation process. The model for each speed was obtained by taking the average force of the 15 insertions at each point starting from the start of relaxation to the end of the shortest relaxation time for those 15 insertions. The average force was then plotted and fit with an exponentially decaying curve.

2.4. Modeling and validation

2.4.1. Finite element modeling of needle puncture

A 3D model of the liver sample was built using ABAQUS (Version 6.3) software. The purpose of modeling the needle insertion task in ABAQUS is to extract the necessary soft tissue parameters, such as the local effective modulus and surrounding tissue deformation, to provide to the real-time graphics community for simulating the procedure. The ABAQUS model contains a global mesh of 34,749 (1 cm^3, eight node) solid linear brick elements with incompatible modes. The mesh is refined in the areas of the bead locations such that a bead can be represented by a node in the model with the same coordinates. The mesh is also refined in the area of needle insertion to a size of $0.05 \times 0.05 \times 0.05$ cm^3. This allows for the needle tip to be represented by a 1 mm^2 section of nine nodes. The actual 18-gauge needle used in the experiments has a diameter of 1.27 mm. The model was constrained so that it mimicked the experimental setup. In the model, the top and bottom side edges were encastered, leaving the front, side, and back face free to distort. The boundary conditions also accounted for the portion of the front of the tissue that is unconstrained due to the shape of the sample (see Fig. 4). The nine nodes representing the needle tip are displaced uniformly under the assumption of uniform load distribution up to the point of puncture and in the direction of puncture. Using an iterative algorithm, we were able to compute the local effective modulus which represents the localized deformation resistance of the soft tissue. The local effective modulus (LEM) was then used in the finite element model to obtain the local tissue deformation and predicted bead displacements due to needle puncture. Fig. 6 shows the deformed 3D ABAQUS model with the refined mesh. DiMaio (DiMaio and Salcudean, 2002) used a similar approach to obtaining the material properties of tissues. After providing force input at the insertion node in the model, DiMaio found the material properties, E and υ, that minimizes the squared error between measured and predicted node positions on the surface of the model. We input

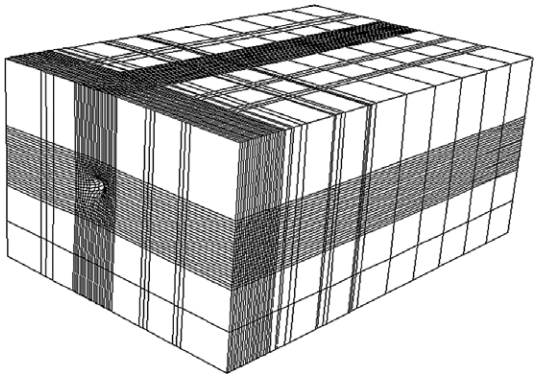

Fig. 6. Initial 3D ABAQUS model for needle puncture with generic geometry. The mesh in the area of the needle puncture site and the bead locations is refined to create much smaller elements.

the displacement at the nine nodes representing the needle tip into our model and find the parameter E that minimizes the error between the experimental forces and the model forces. The calculation is described in the following section.

2.4.2. Calculation of the local effective modulus

Using the experimental puncture force obtained for each insertion and the corresponding tissue displacement, we were able to compute the local effective modulus for puncture. The initial local effective modulus of arbitrary magnitude E_1, assigned to each element of the model, and a Poisson's ratio of 0.499 were chosen in our algorithm. For each puncture, the nine needle nodes were given an experimentally measured displacement $\Delta U^{\exp}$. The computed change in force, ΔF^{FEM}, from the displacement at the nodes was compared with the change in force, ΔF^{EXP}, measured experimentally. If the computed ΔF^{FEM} was more than 1% off from the ΔF^{EXP}, we automatically revised the assumption of E_1 and continued the iteration until convergence was achieved. The final E_1 value so determined is the local effective modulus of the tissue during the puncture. Fig. 7 demonstrates this approach. While the local effective modulus for puncture is applied to the entire model during the computation it is only valid for describing the local area surrounding the tissue site as described in the later sections. New LEM values will be calculated for multiple sections in the tissue following a similar approach to the LEM for puncture. Our eventual goal is to develop a complete finite element computational model that will contain LEM values assigned to elements within the appropriate sections for accurately describing the force versus displacement behavior locally inside the tissue.

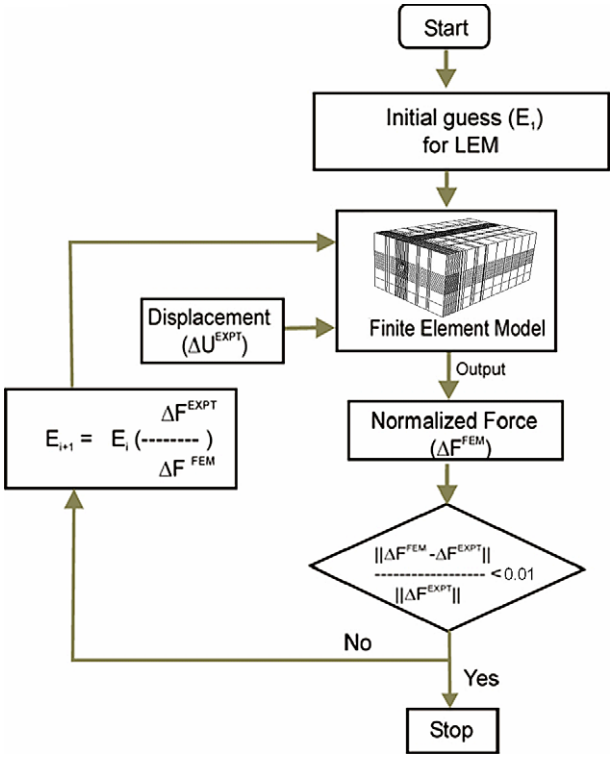

Fig. 7. Flow chart for the determination of the local effective modulus (LEM). Linear elastic FEM analysis is used with a Poisson's ratio of 0.499 and an initial local effective modulus of arbitrary magnitude E_1. The nodes representing the needle tip are given an experimentally measured displacement $\Delta U^{\exp.}$. The computed ΔF^{FEM} from the displacement at the nodes was compared with the ΔF^{EXP} measured experimentally. Using the initial effective modulus E_1, iterations are performed to obtain the ΔF^{FEM} equal to ΔF^{EXP}. The final E value determined is the local effect modulus, $E^{\mathrm{effective}}$, of the tissue during the puncture.

2.4.3. Validation of the local effective modulus obtained from ABAQUS

The purpose of validation was that given a local effective modulus of puncture for a given tissue sample, the model should be able to predict the forces experienced by the needle tip for any deformation prior to puncture. We validated our ABAQUS iterative approach for determining the local effective modulus (LEM) of puncture by using the ABAQUS model to predict the needle tip reaction forces for an arbitrary needle insertion task in a soft tissue sample. We performed four sample needle insertion tasks and computed the LEM for puncture for these needle insertion tasks. We then averaged the LEM value and used that as the input for an arbitrary needle insertion task. Hence, in the 5th insertion on the same sample we input the displacement and the average LEM value into our ABAQUS model and computed the resulting force ΔF^{FEM}. This force ΔF^{FEM} was compared with the experimental ΔF^{EXP}.

2.4.4. Comparing local and global tissue deformation

It is of great interest for accurate needle insertion simulation to model not only the local tissue deformation at the needle site but also to model the global tissue deformation as well. To understand the size of the area of the tissue for which the local effective modulus is valid for estimating tissue forces and deformation during puncture, we used the local effective modulus as the global tissue elastic modulus. We compared the experimental displacement of 15 beads nearest the needle tip as shown in Fig. 8 and compared it with the predicted displacement of the 15 beads represented in the ABAQUS model. Outside of the 15 bead area, tissue movement was negligible during a typical initial puncture of the tissue. Each data set comes from the same tissue

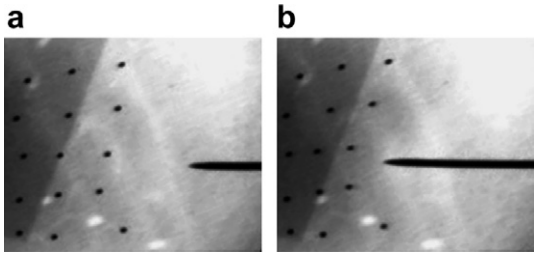

Fig. 8. Top view of the X-ray image: (a) as the needle touches the tissue and (b) just before puncture. Fifteen beads closest to the needle tip are tracked during puncture. The displacement data is used for the finite element model validation.

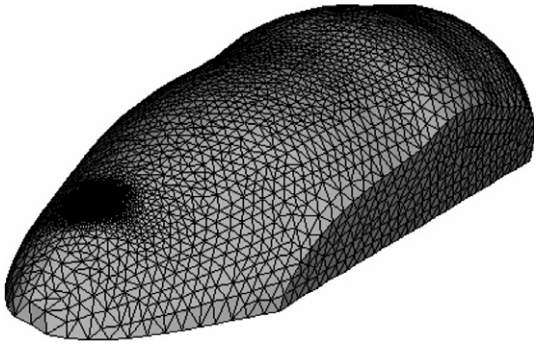

Fig. 9. Realistic 3D ABAQUS model generated from X-ray and physical measurement. The mesh is refined in the needle puncture site and the bead locations.

sample but different needle puncture positions. The initial ABAQUS model shown in Fig. 6 was used for an initial analysis and then a more specific geometrically accurate model with more appropriate boundary conditions was used for the same analysis. The new model geometry shown in Fig. 9 was created using measurements from X-ray images and physical measurements. The boundary conditions assigned to the model were assigned to match the experimental conditions as close as possible.

The ability to image the internal tissue movement can be used as a tool for validating model results and quantifying tissue and needle interaction inside the tissue specimen.

2.5. Simulation

We used a 7-DOF haptic feedback device to replay the forces encountered during experimental measurements of needle insertion and withdrawal tasks. The purpose of the simulation is to demonstrate an integration of this work with a suitable haptic feedback device for training surgeons to perform needle insertion tasks. The haptic feedback device has 4 degrees of force feedback capability and 7 degrees of position feedback capability (see Fig. 10) (Tholey and Desai, 2005). The device consists of a closed-kinematic chain with two parts, a user interface and a spatial

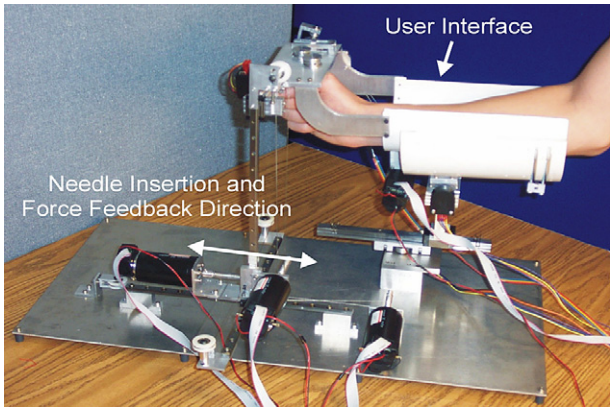

Fig. 10. Haptic device used for the needle insertion simulation.

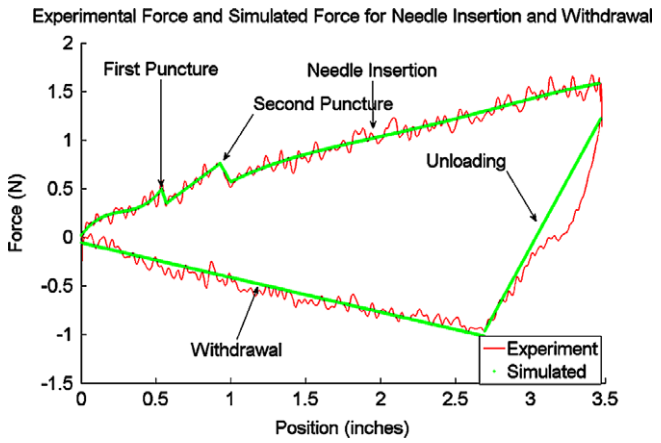

Fig. 11. Experimental force profile matched with the simulated force profile. The experimental force is a sample force profile from an ex vivo needle insertion and withdrawal into soft tissue. The simulated force profile is used as the force feedback to the user through the haptic device for the needle insertion simulation.

force feedback mechanism that are connected together via a universal joint. The user interface is a hand and forearm rest that contains a yaw, pitch, roll, and linear motion using passive joints with encoders. A grasping mechanism mounted at the end effector of the user interface enables the user to control grasping/parting tasks and also display forces to the user from these tasks. The spatial force feedback mechanism provides force feedback along the X, Y, and Z directions, respectively. The sampling rate of the force signals being sent to the haptic device is 500 Hz. Since the force and position information is recorded from actual needle insertion experiments, replaying this data on the haptic device helps to assess the transparency of the device (after modeling the friction in the transmission) and the realism of the needle insertion task. Fig. 11 shows the experimental force profile and the modeled force profile for a typical needle insertion event. The force profile shows two puncture events which occur on the surface of the tissue. A puncture event comprises of initial deformation (leading to a rise in the force) followed by puncture (sudden drop in the force). The two puncture events are due to the fact that the needle tip and cannula do not have a seamless boundary (see Fig. 5). In our preliminary work, the haptic device is capable of replaying the forces for both needle insertion and withdrawal; however, there is no visual feedback since we have not yet developed the graphics capability.

3. Results

3.1. Needle deflection and marker movement

Fig. 12 shows the trajectory of the needle through the soft tissue during needle insertion and withdrawal. Deflection of the needle tip from the straight line trajectory was observed during every needle experiment. Table 2 shows the average deflection for the insertion speeds of

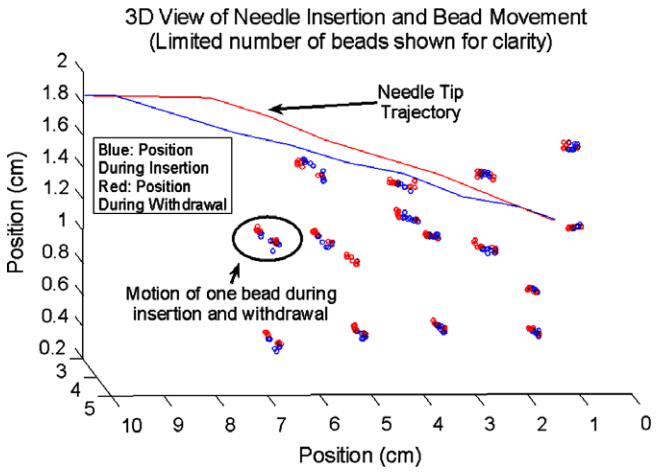

Fig. 12. 3D bead movement during needle insertion and withdrawal. The solid line represents the needle tip trajectory through the tissue. Each cluster of data points represents the 3D movement of a bead during needle insertion and withdrawal. A limited number of beads are shown in the figure for clarity. Forty beads are tracked during a single insertion experiment.

Table 2
Needle deflection from the initial straight line trajectory

Speed (mm/s)	1.016	12.7	25.4
Average deflection (mm)	4.24	5.48	6.21
±SD (mm)	±1.27	±1.38	±1.11

1.016 mm/s, 12.7 mm/s, and 25.4 mm/s. Although within one standard deviation of each other, deflection was found to increase slightly with an increased needle velocity. The maximum deflection from the straight line needle trajectory seen in our experiments was found to be 7.84 mm.

Fig. 12 also illustrates the movement of the markers during a typical needle insertion and withdrawal in soft tissue. Each cluster in Fig. 12 represents the area covered by the movement of a bead with the surrounding tissue. For clarity, we have only shown a small subset of beads actually used in the experiment. For this sample data set, the needle was inserted at 12.7 mm/s to a depth of approximately 95 mm. Each bead has a corresponding blue color for its position during insertion and red color for its position during withdrawal. As seen from the figure, there is significant movement of the bead during insertion and withdrawal of the needle from the tissue. Beads closest to the needle path showed the largest range of movement while the movement of beads farther away from the needle path was less. The estimated movement of the beads is used to validate a finite element model to predict soft tissue deformation during needle insertion and withdrawal task.

Tracking results for the needle tip are displayed in Table 3 which shows the comparison of the actual versus measured magnitude of movement of a needle using our tracking algorithms. The tracking algorithm is shown to be accurate to within $2.09 \pm 1.61\%$ of the actual movement.

Table 3
Comparison of the measured distance (magnitude) traveled by the needle tip movement with the actual distance (magnitude) traveled

Insertion	Measured magnitude distance (in.)	Actual magnitude distance (in.)	% Error
1	3.5950	3.4683	3.65
2	1.3674	1.3058	4.72
3	3.4701	3.4803	0.29
4	1.1902	1.1671	1.98
5	3.4502	3.4689	0.50
6	1.3116	1.2744	2.92
7	3.5501	3.4819	1.96
8	1.6435	1.6148	1.78
9	3.6301	3.4821	4.25
10	3.4485	3.4697	0.92
11	0.9218	0.9249	0.34
Average			2.09
±SD			1.61

3.1.1. Effect of bead implantation on experimental data

Fig. 13 shows the needle forces during insertion into a soft tissue specimen with and without implanted beads. The data show that there is no significant difference in the forces due to the implantation of forty 1 mm diameter beads into the tissue.

3.2. Soft-tissue property: forces

3.2.1. Task 1: tissue puncture

Fig. 14 shows the force data during an experimental needle insertion and withdrawal task broken into four sections, puncture, insertion, relaxation, and withdrawal. Fig. 15 illustrates the mean force at the moment of puncture for each liver at various insertion speeds. As seen from the figure, the mean puncture force for each liver sample is within one standard deviation of each other. Table 4 shows the mean puncture force averaged over all liver samples for a particular insertion speed. As the speed increases, the

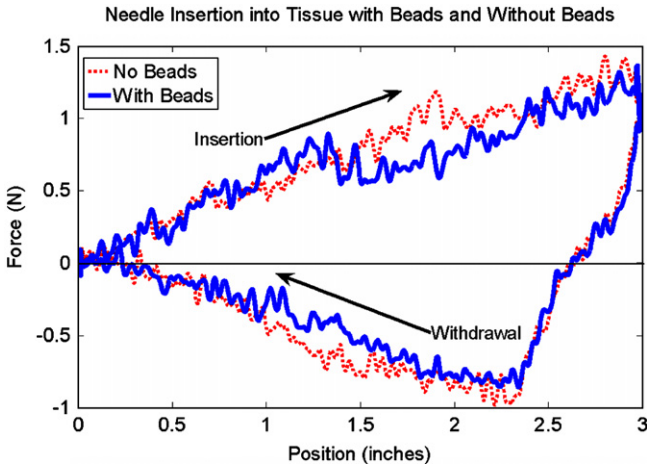

Fig. 13. Comparison of the needle forces for an insertion into a soft tissue specimen with and without implanted beads. Insertion speed was 12.7 mm/s.

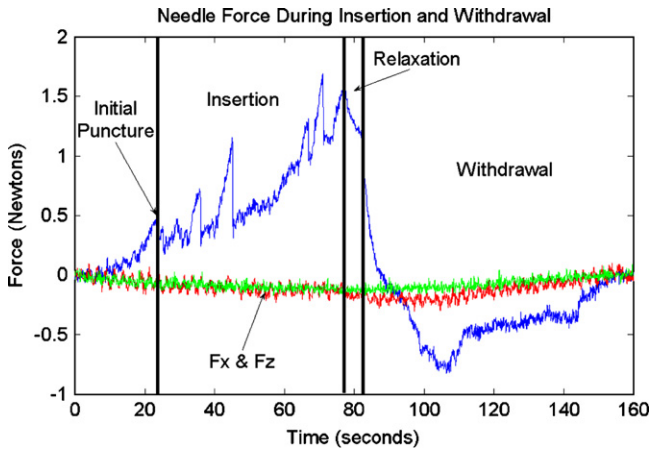

Fig. 14. Total needle forces during insertion and withdrawal. Each phase of the experiment is segmented by a horizontal line through the plot. The data plotted are the needle forces during an insertion and withdrawal in soft tissue at 1.016 mm/s.

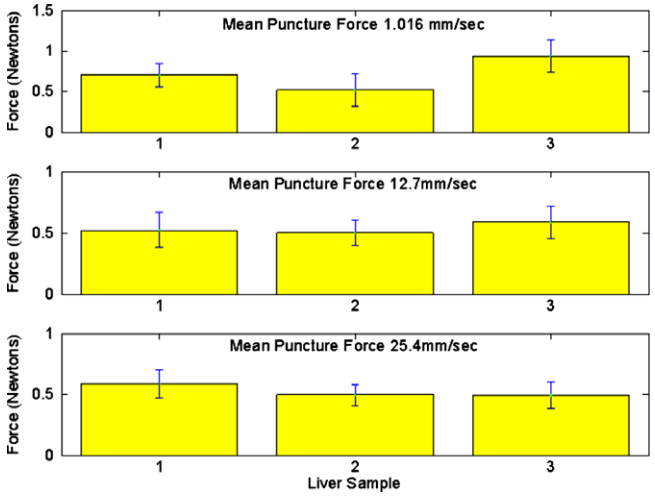

Fig. 15. Mean puncture force for each soft tissue sample at various insertion speeds.

Table 4
Mean puncture force for each insertion speed

Speed (mm/s)	1.016	12.7	25.4
Mean puncture (N)	0.72	0.54	0.53
±SD (N)	±0.25	±0.12	±0.11

mean puncture force decreases, however the values are still within one standard deviation of each other. Fig. 16 highlights 10 major puncture events occurring inside of a soft tissue sample during an insertion at a speed of 1.016 mm/s.

3.2.2. Task 2: needle insertion

Figs. 14 and 17 illustrate our approach to determining the cutting force with a needle insertion and withdrawal sample. The approximate cutting force for puncture was obtained for each of the 45 insertions (3 livers*5 insertions*3 speeds). Using data from Fig. 17 as an example, the approximate cutting force varies around a single force value throughout the insertion, illustrating that the force required to cut through the tissue is fairly constant throughout the specimen. Fig. 18 shows the mean cutting force for each insertion obtained from 15 insertions at each cutting speed.

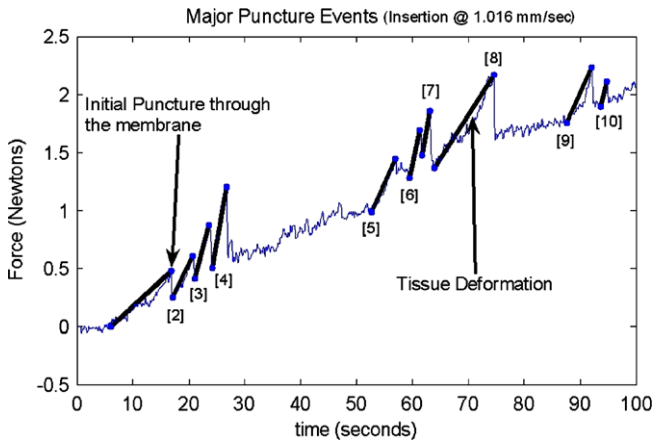

Fig. 16. Major puncture events within a sample of soft tissue during one experimental insertion at 1.016 mm/s. A major puncture event occurs when the needle encounters some obstacles inside the tissue during insertion. A puncture event is comprised of a rise in the force and then a sudden drop in force representing the moment of puncture. During a puncture event, the tissue is no longer being cut and is assumed to be deforming at the same rate as the needle tip velocity.

There is a difference between the approximate cutting force for insertion at 1.061 mm/s, 12.7 mm/s and 25.4 mm/s. Table 5 shows the mean cutting force averaged across all liver specimens for a given cutting speed. The mean cutting force at the insertion speed of 1.016 mm/s insertions was lower than the cutting force at higher insertion speed. However, the cutting force for each of the 45 needle insertion and withdrawals had a much greater variation around the mean cutting value as the insertion speed decreased. The average variation around the mean cutting force was 0.1276 N, 0.1454 N and 0.3233 N for each one of the 15 insertions at speeds of 25.4, 12.7, and 1.016 mm/s, respectively. As the insertion speed increased, the variation of the force around the mean cutting force was less.

3.3. Soft-tissue property: tissue relaxation

3.3.1. Task 3: tissue relaxation

Fig. 19 illustrates the relaxation of the tissue occurring based on the force data after the needle has been fully inserted and held into place. Fig. 20 represents the relaxation of the tissue observed through tissue movement. The figure is of a top view of one bead inside the tissue close to the needle path during a needle insertion and withdrawal task. Relaxation of the tissue can be seen after the needle has been fully inserted and held in place and also after complete withdrawal of the needle. Fig. 21 shows the average

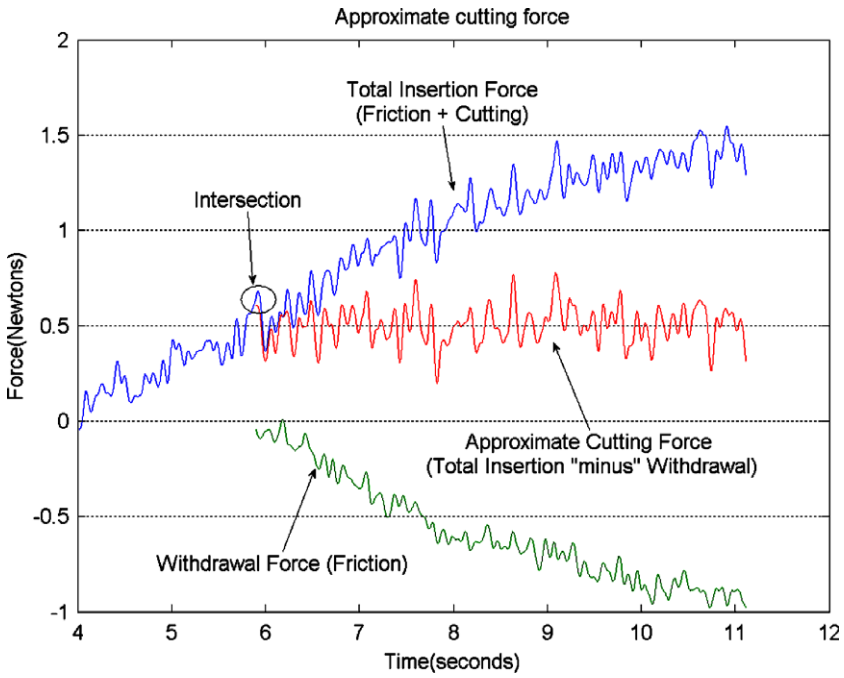

Fig. 17. Plot of the approximate cutting force during needle insertion for an insertion speed of 12.7 mm/s. The withdrawal force is subtracted from the total insertion force to obtain the approximate cutting force.

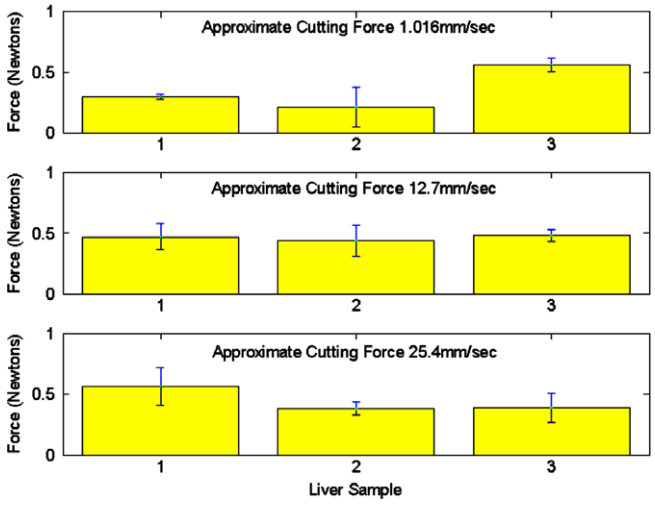

Fig. 18. Approximate cutting force for various insertion speeds.

relaxation curves for the three insertion speeds, each fitted with an exponentially decaying model. The following equations are the exponential fit for the relaxation process for 1.016 mm/s, 12.7 mm/s and 25.4 mm/s needle insertion speeds:

Table 5
Mean cutting force for each insertion speed

Speed (mm/s)	1.016	12.7	25.4
Mean cutting (N)	0.36	0.46	0.44
±SD (N)	±0.18	±0.09	±0.14

$$1.016\,\text{mm/s}: \quad y = 0.3799 * \exp(-1.0841 * t) + 0.9932 \tag{2}$$

$$12.7\,\text{mm/s}: \quad y = 0.1886 * \exp(-0.9865 * t) + 1.0883 \tag{3}$$

$$25.4\,\text{mm/s}: \quad y = 0.2056 * \exp(-0.8150 * t) + 0.9702 \tag{4}$$

The relaxation of the tissue shows a slight trend towards an increase in "steepness" of the decay as the insertion velocity of the needle decreases. The average starting relaxation force value increases as the insertion velocity of the needle decreases.

3.4. Modeling and validation

3.4.1. Determination of the local effective modulus (LEM)

Fig. 22 shows the mean E_1 value obtained for each of the three liver samples at various insertion speeds.

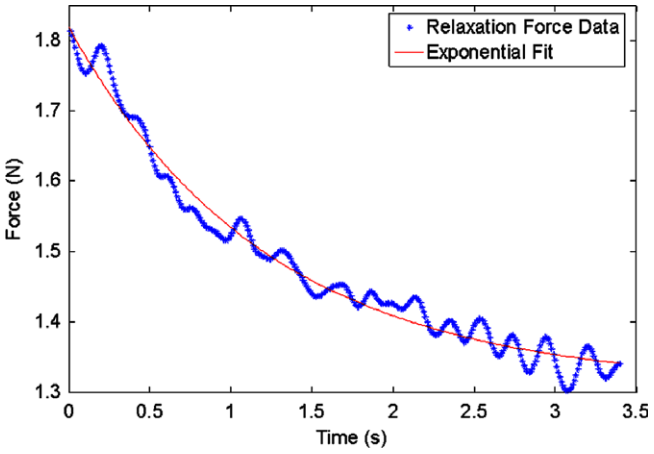

Fig. 19. Force decay during relaxation of the tissue after the complete insertion of a needle.

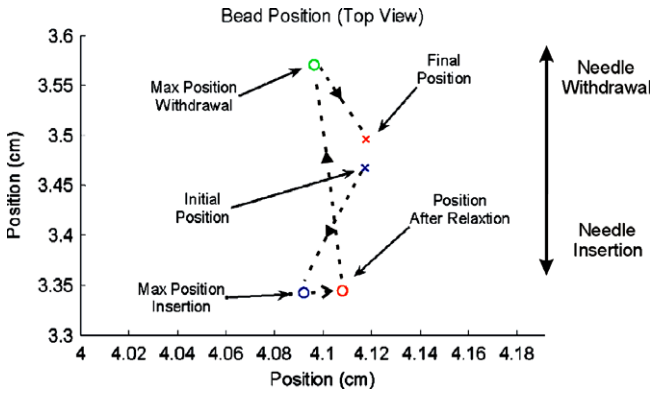

Fig. 20. Top view of the bead movement during relaxation of the tissue after needle insertion and withdrawal. The max position during insertion shows the location of the bead before relaxation of the compression of the tissue and the max position during withdrawal shows the location of the bead before relaxation of the tension in the tissue.

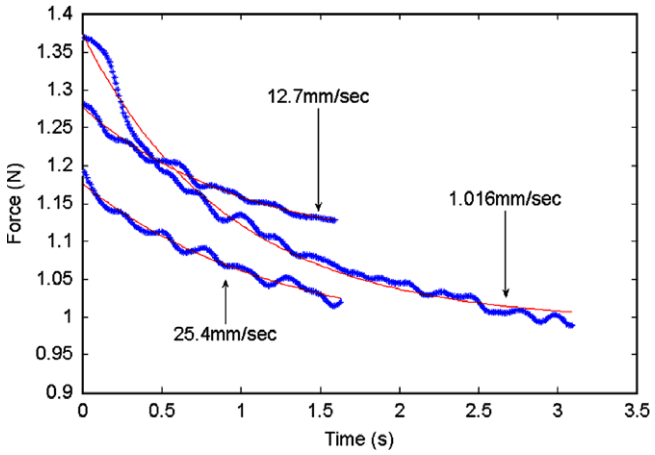

Fig. 21. Averaged force plots during tissue relaxation at various needle insertion speeds.

Table 6 shows the mean LEM values for each insertion speed. The local effective modulus is used in the FEM model to obtain the local stresses and strains of the soft tissue during needle puncture, the needle tip reaction forces, and local tissue deformation.

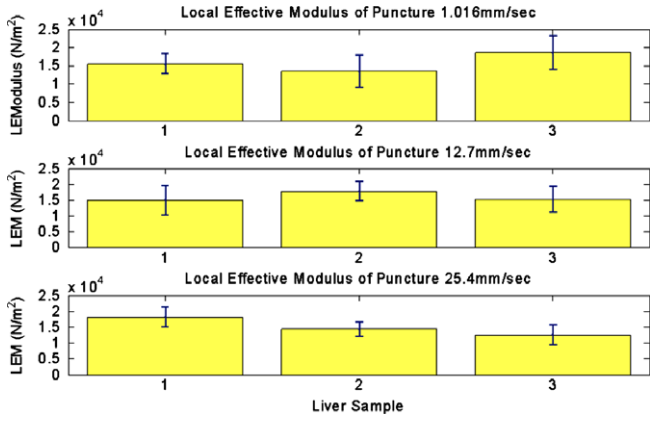

Fig. 22. Local effective modulus for initial puncture at 1.016 mm/s, 12.7 mm/s, and 25.4 mm/s insertion speed.

Table 6
Mean LEM values for each insertion speed

Speed (mm/s)	1.016	12.7	25.4
Mean LEM (N)	15 893	16 119	15 087
±SD (N)	±4330.3	±3865.8	±3564

Table 7
Comparison of the experiment with ABAQUS needle tip forces and LEM for puncture

	Experiment	ABAQUS
Force (N)	0.51	0.59
LEM (N/m^2)		1.43 (Average)

The average LEM used for validation is shown in Table 7 with the predicted needle reaction force value for a given displacement of 17 mm. The experimentally measured force for that displacement is also given in the table.

3.4.2. Comparison of the local and global modulus

In Fig. 23, the results from the comparison of the estimated bead position with the measured position just before needle puncture can be seen for the four trials using the initial ABAQUS model shown in Fig. 6. Comparison of the displaced distance predicted by ABAQUS with the actual displacement extracted from the C-arm images shows that the average error magnitude is 1.88 mm ± 1.55 mm. Fig. 24 shows the results from one trial using the realistic geometry model shown in Fig. 9. The average error magnitude is 0.87 mm ± 0.68 mm. Comparison of the two models show a 53% reduction in error when using the realistic geometry model of Fig. 9 for predicting the bead displacement compared to a rectangular tissue model shown in Fig. 6.

3.5. Simulation

From a typical needle insertion and withdrawal task, we can model the force versus position profile, such as the simulated profile shown in Fig. 11. After the completion of full insertion, the force drops to a lower absolute value compared to the force at full insertion, due to tissue relaxation. The point corresponding to the peak in force magnitude for needle insertion is joined by a straight line to the point corresponding to the onset of needle withdrawal. Subsequent intermediate points are parallel to this line for loading and unloading phase of needle insertion and withdrawal task. These loading/unloading phases are shown because the user may decide to do partial insertion and withdrawal rather than the full insertion and the haptic device should be able to replay those insertion and withdrawal forces. Fig. 25 illustrates these insertion and withdrawal forces that are replayed to the user through the haptic feedback device.

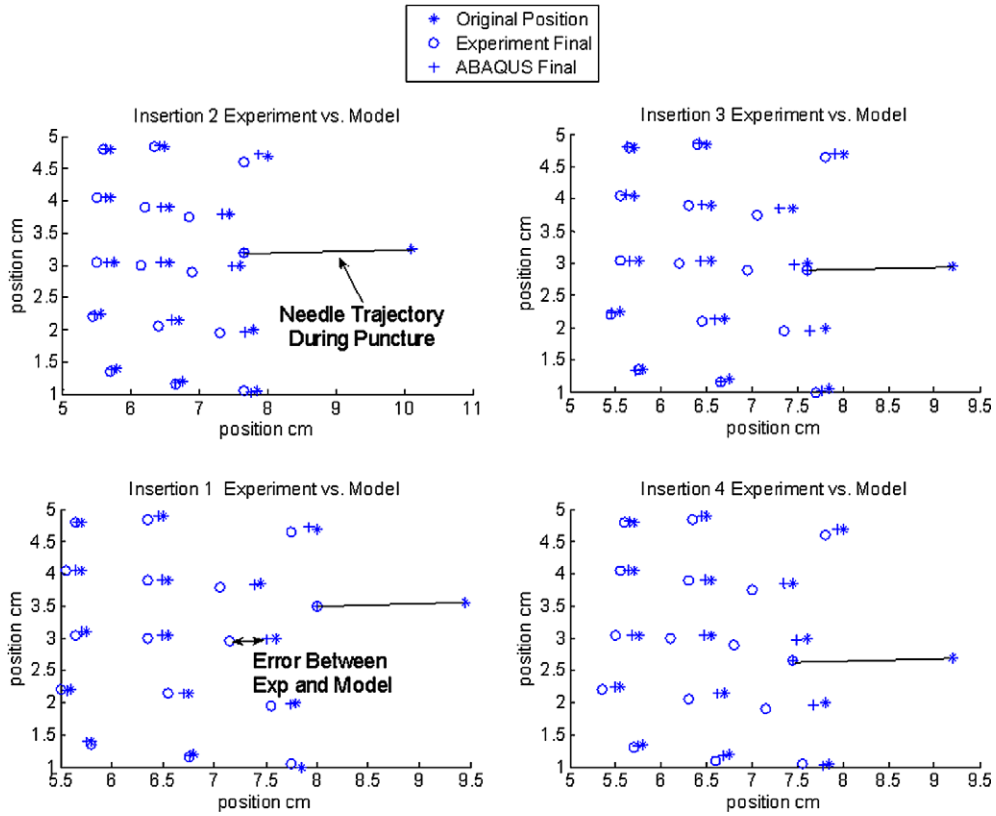

Fig. 23. Bead displacements due to puncture estimated by the initial generic geometry finite element model and compared with the experimental displacement. Four separate puncture data sets are plotted. Each data set comes from needle puncture on the same soft tissue specimen. The experiment needle position during puncture is used as the input to the finite element model. The largest error is located at beads closest to the needle tip.

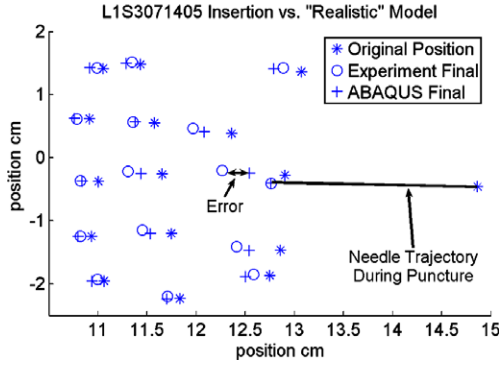

Fig. 24. Bead displacements due to puncture estimated by the realistic geometry finite element model compared with the experimental displacement.

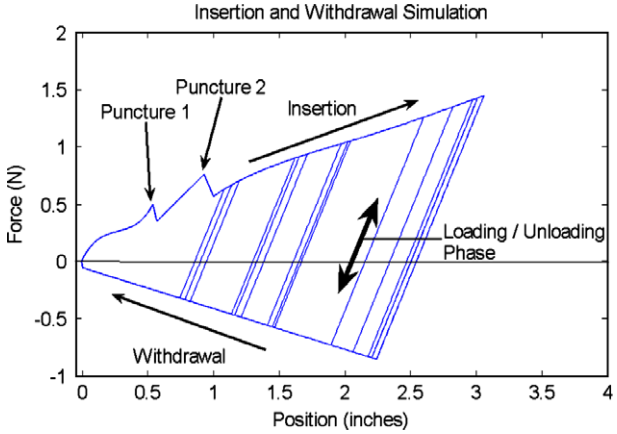

Fig. 25. Forces experienced by the user during a sample needle insertion simulation. The multiple loading and unloading phases in the plot represent the forces relayed to the user when the needle has changed direction from insertion to withdrawal (and vice versa) at different depths within the tissue.

4. Discussion

4.1. Needle movement

Needle deflection is important to measure and predict, especially for training radiation oncologists to accurately place seeds in the prostate during a prostate brachytherapy procedure. In a typical prostate brachytherapy task the needle can deflect as much as 10 mm from the initial insertion point as it travels through the perineum, fat, muscle, and then prostate (Cormack et al., 2000). This deflection of the needle sometimes requires recomputation of the dosage information for radioactive seed placement. During each insertion, we observed a difference in the needle's trajectory from its initial straight line trajectory into the tissue. Most of the deflection was caused during the initial

puncture due to the force produced by the tissue deformation although some deflection was also caused by the inhomogeneity of the soft tissue, generating asymmetric forces on the needle. An increase in the needle velocity showed a slight increase in the needle deflection within the tissue. The increase in deflection may be a product of the higher cutting forces generated at the needle tip when inserting at faster speeds.

4.2. Effect of bead implantation on experimental data

The fiducials that we have implanted into the soft tissue have been shown to have very little effect on the force profile when compared with the tissue without beads inserted. An important item to note is that due to the nature of biological tissues, the forces will not be the same for each insertion; even for multiple insertions on the same specimen with no beads. The implanted force profile shown in Fig. 13, does not lie outside the range of the variation between force profiles for multiple insertions into the same tissue specimen without implanted beads. From this, we can make the assumption that the properties of the tissue do not change due to the implantation of the beads.

4.3. Needle–soft-tissue interaction forces (Task 1: tissue puncture)

We have shown that a good approximation of the puncture force based on only force data is the point where the total insertion force reaches the approximate cutting force described in Section 3.2.1 (see Fig. 17). This approximation correlates very well with the time of puncture obtained from image analysis. Alternatively, if the force data does not contain much noise and the puncture is significant, the puncture force can be seen as the point at which the force suddenly drops after rising, signifying the compression of the tissue and then quick release of the compression right after puncture. The data from the force profiles for each puncture event can be used to obtain the local effective modulus of the liver sample at each location of puncture events inside the tissue.

The speed of needle insertion affects the deformation at the tissue site and the force at the needle tip. For lower puncture forces and less tissue deformation during puncture, the needle should be inserted at faster speeds.

4.4. Needle–soft-tissue interaction forces (Task 2: needle insertion)

The speed of insertion has also been shown to affect the reaction forces acting on the needle during needle insertion. The approximate cutting force was shown to increase however, the increase in needle speed lead to less force variation around the mean cutting force. Less variation demonstrates that cutting was smoother for faster insertion speeds, and the needle was less prone to experiencing major puncture events inside the tissue. However, as shown earlier, higher cutting forces lead to higher needle deflections so it is a trade off between smoother cut and straightness of the needle trajectory. There are few researchers working on developing new needle insertion techniques such as rotating the needle during insertion to minimize this deflection (Alterovitz et al., 2005).

4.5. Tissue relaxation (Task 3)

Similar to the approximate cutting force, the relaxation portion of the force profile has also been shown to be affected by the rate of needle insertion. At slower constant needle insertion velocities, the total force at the start of needle insertion tends to start higher than the faster insertion velocities. One possible explanation of the increased starting relaxation force can be attributed to the needle dragging more of the tissue as the velocity decreases. As discussed earlier, the needle tends to create more puncture events inside the tissue as the velocity decreases. These puncture events cause the tissue to compress which would explain the higher starting force value as the velocity of the needle decreases due to the increased amount of compression of the tissue by the end of the insertion process. In addition to being dependent on needle velocity, the relaxation effect will be affected by tissue stiffness, needle lubrication, position, orientation and deflection of the needle. Since the tissue is non-homogeneous, relaxation will be effected by the above mentioned factors across the specimen for the same needle type and the needle position within the tissue. Even for an experiment of this tissue type, we saw a large standard deviation for fixed insertion velocities.

4.6. Determination of the local effective modulus (LEM)

The local effective modulus is fairly constant throughout each insertion speed and liver specimens, indicating that there is little change in the properties of the tissue during the initial puncture at different speeds and between tissue specimens. This may be due to the small surface area of the needle deforming the tissue compared to the size of the specimen.

The local effective modulus can be used to predict the needle tip reaction forces for a given displacement during puncture of a soft tissue sample. From Table 7, it is seen that the ABAQUS computed reaction force is relatively close to that of the measured experimental force for a given displacement. This result validates our approach for using the local effective modulus of puncture to describe the needle puncture site.

4.7. Comparison of the local and global modulus

The local effective modulus was also used to predict the local tissue deformation around the tissue puncture side. With the initial ABAQUS model, much of the error found can be attributed to the difference in boundary conditions

from those of the experiment. The tissue at the puncture site was not constrained (see Fig. 4) properly due to limitations in the experimental setup, compared to the ABAQUS model where the tissue was constrained at the boundaries (see Fig. 6). While the error can be minimized by applying a scaling factor to the ABAQUS results (see Fig. 23), we have shown that for the initial model (see Fig. 6), the local effective modulus is only valid if applied to the immediate location of the needle tip. Conducting the same analysis using the new model based on the geometry of the soft tissue sample and applying boundary conditions matching those of the experiment (see Fig. 9), we have shown that the local effective modulus can be used to predict the local tissue movement surrounding the puncture site with much less error than the initial model. Further reduction in the error for the predicted bead displacement may require the use of a hyperelastic model with the LEM rather than the current linear elastic approach. Hyperelastic models, such as the Ogden model, have been shown to better represent soft tissue behavior under applied force compared to linear elastic models.

5. Conclusion

This study demonstrates a unique approach for estimating needle and soft tissue interaction. Using a dual C-arm fluoroscope setup and implanted radio-opaque markers, we can obtain in real time, 3D needle trajectory and internal global and local tissue deformation during needle insertion into soft tissue. Information such as the time of tissue puncture, various internal puncture events, tissue relaxation, and the start of kinetic friction during withdrawal can be extracted from the X-ray images by tracking the relative velocities of the implanted markers with the tip of the needle. Utilizing this image information along with the force information, we can find the local effective modulus during puncture and puncture events in the tissue. The approximate cutting force was found by subtraction of the total insertion force from the friction force. This cutting force can be used to characterize how much energy is required to cut at any location within the tissue. We have validated the accuracy of our approach to determine the local effective modulus during needle puncture of soft tissue. We have also developed a procedure for validating finite element models of soft-tissue interactions with needles by comparing the measured 3D implanted fiducial displacements with the displacement estimated by the finite element model. To further enhance the simulation we have integrated a 7 degree-of-freedom haptic feedback device to display the realistic forces during needle insertion and withdrawal.

While the actual results presented such as local effective modulus, puncture force and cutting force are specific to that of excised, unperfused porcine liver tissue, the procedure for obtaining these results can be applied to the study of all soft tissue and systems of soft tissue such as needle insertion through perineum, fat, and muscle, for example. Studies will have to be conducted to verify if properties such as the independence of LEM from the needle insertion rate is a valid statement for soft tissue samples other than the liver. Work on homogeneous clear phantom tissue has three major benefits when analyzing needle and tissue interaction, namely, homogeneity of the sample, easy visualization of the internal tissue and needle during insertion, and prior knowledge of the material properties of the tissue sample. The forces acting along the shaft of the needle during insertion and other needle tissue interactions can be extracted using this information. Our setup has enabled the visualization of the internal tissue and needle, during insertion into soft tissue and we have developed procedures for obtaining material properties like the LEM during needle puncture. While the local effective modulus for puncture can relatively accurately predict the needle tip reaction force and the local tissue deformation of the puncture site, it may not be valid to describe the tissue deformation and reaction forces further inside the tissue. Other techniques are currently being developed using our setup to analyze the needle and soft-tissue interactions and to find properties such as the LEM past the puncture event without the benefits of homogeneity of the tissue and prior knowledge of the material properties. Future work will also require a closer evaluation of the deformation of the surface of the tissue near the needle insertion point and studies on needle insertion into different soft tissue samples and systems of soft tissues. The simulation will also be enhanced to include a needle velocity component, the visco-elastic properties of the tissue and a realistic graphical user interface. As for in vivo studies, the goal is to do ex vivo model first for the entire process. In vivo work also will be dependent on the procedure specific needle insertion task, whether it is prostate brachytherapy, liver biopsy, or epidural needle insertion procedure.

Acknowledgements

This work was supported in part by National Science Foundation CAREER Award IIS 0133471, NSF ITR Award 0312709 and the Beukenkamp Endowment for Prostate Cancer in Drexel University College of Medicine, Department of Surgery. We thank Dr. Waqus Anjum, Dr. Justin Chandler, and Jeff Justin for their valuable help in conducting dual C-ARM experiments and C-arm calibration. We thank Gregory Tholey for allowing us to use the haptic feedback device for our needle simulation trials.

Appendix A. C-arm fluoroscope calibration

To obtain the accurate locations of the markers in the C-arm images, distortion and magnification of the images has to be measured and accounted. The quality of a C-arm image is relatively low due to two main causes of distortion: pincushion distortion and S curve distortion (Hendee and Ritenour, 2002). Pincushion distortion in our setup is caused from the mapping of a flat surface onto a curved

input phosphor of the image intensifier (detector) (see Fig. A1). The S curve distortion is caused by the deflection of the electrons due to the earth's magnetic field and it is dependent on the angle of the image intensifier in the magnetic field. In our experiments, this effect was minimal and hence it was neglected. For each C-arm used in the experiments, a calibration grid consisting of equally spaced patterned holes was imaged. A number of papers have been published using a similar method to correct for the distortion caused by the image intensifier (Rudin et al., 1991; Fahrig et al., 1997; Cosby and Leszczynski, 1998). Using Matlab, the centroids of the patterned holes were extracted. The pattern in the center of the image (within a 10 pixel window) is undistorted and the radial distance to the centroids of these holes from the center of the image was used as the "true" distance. Fig. A2 shows the centroids of the pattern marked with "O" and the correct distance marked with "+". As seen from the figure, there is a significant variability as the distance from the center increases. A second-order polynomial equation, as seen in Fig. A3, was fit to the error between the true distance to the centroids and distorted image distance.

We get the following equations for each C-arm fluoroscope:

$$\text{OEC 9600}: \quad y = 0.0006r^2 - 0.0706r + 1.6171 \qquad (A.1)$$

$$\text{OEC 7700}: \quad y = 0.0002r^2 - 0.0175r + 0.5651 \qquad (A.2)$$

where y is the error in pixels between the correct and distorted position and r is the radial distance of the distorted point from the center of the image. Applying the polynomial to the image corrected the distortion as shown in Fig. A4. The effect of the correction is most noticeable at the boundary. Each C-arm required separate polynomial corrections (Eqs. (A.1) and (A.2) for C-arm fluoroscope model OEC 9600 and OEC 7700, respectively).

Magnification of points in the image also had to be considered. A C-arm can be modeled similar to a pin hole camera. As seen in Fig. A1, two markers, one located closer to the X-ray source than the other, traveling the same distance, the closer marker will travel more pixels in the image than the marker farther from the source. Magnification calibration for the two C-arms was conducted by imaging a radio-opaque ruler at various distances from the X-ray

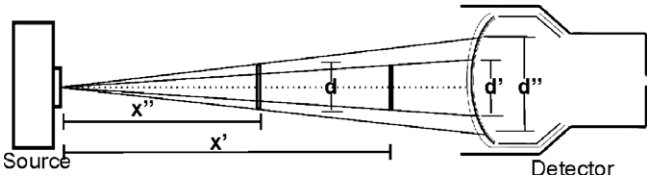

Fig. A1. Schematic of a C-arm fluoroscope imaging two same size objects x' and x'' distances from the X-ray source. The C-arm is modeled as a pinhole camera where X-rays are emitted from the source and received at the detector. Due to the pinhole effect, images closer to the source are magnified. Also the curvature of the surface of the detector leads to pincushion distortion of the X-ray image.

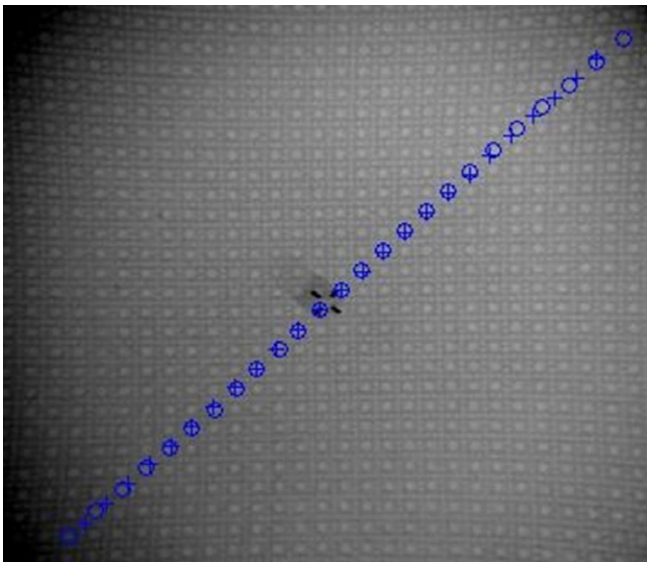

Fig. A2. Equally spaced patterned aluminum sheet imaged using the C-arm. The correct centroid locations of the patterned holes are marked with a (+) and the distorted locations of the centroids are marked with a (O). The error increases with the radius from the center of the image.

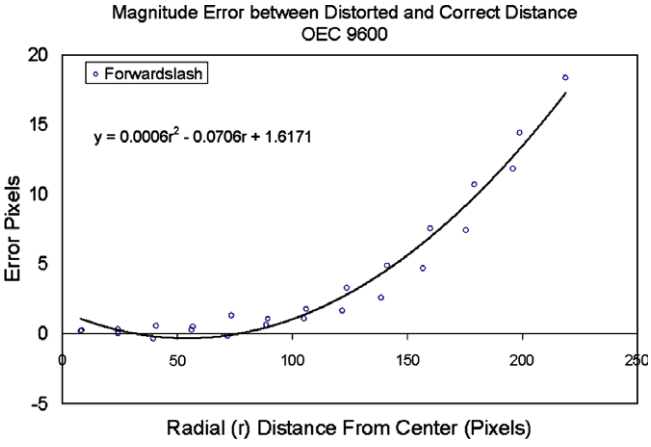

Fig. A3. Second-order fit of the error (OEC 9600) between the distorted and corrected distances to the calibration grid centroids. Forward-slash represents the "forward-slash" diagonal of the centroids in the image. The second-order fit of the error for the OEC 7700 is found following the same approach.

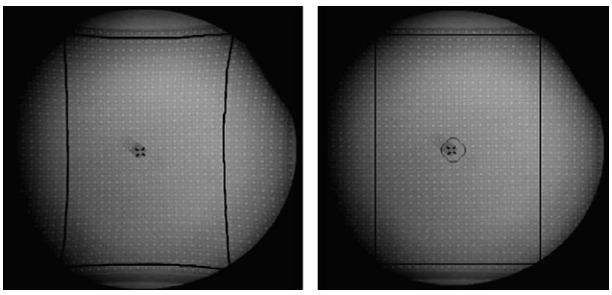

Fig. A4. (a) Distorted X-ray image and (b) corrected X-ray image. Four lines in each image are enhanced by black to clearly show the correction in the distortion.

source. For each C-arm, the pixel to mm conversion as distance from the X-ray source increased was fit with a second-order polynomial where p is the number of pixels per mm and x is the marker distance from the source in cm:

$$\text{OEC 9600}: \quad p = 0.00078402x^2 - 0.1093x + 5.5858 \quad \text{(A.3)}$$

$$\text{OEC 7700}: \quad p = 0.00050624x^2 - 0.091541x + 6.0893 \quad \text{(A.4)}$$

Each C-arm requires two separate corrections; the first correction (Fig. A3) resolves the pincushion effect of the image and does not depend on the distance (x) from the source of the object being imaged but does depend on the radial (r) distance of the object from the center of the image. The second correction (Eqs. (A.3) and (A.4) for C-arm fluoroscope model OEC 9600 and OEC 7700, respectively) compensates for the magnification of the image as the object moves away from the source.

References

Alterovitz, R., Lim, A. et al. 2005. Steering flexible needles under markov motion uncertainty. In: Proceedings of the IEEE/RSJ International Conference on Intelligent Robots and Systems.

Alterovitz, R., Pouliot, R., et al., 2003. Simulating needle insertion and radioactive seed implantation for prostate brachytherapy. Medicine Meets Virtual Reality 11.

Brett, P.N., Harrison, A.J., et al., 2000. Schemes for the identification of tissue types and boundaries at the tool point for surgical needles. IEEE Transactions on Information Technology in Biomedicine, 30–36.

Brouwer, I., 2001. Measuring in vivo animal soft tissue properties for haptic modeling in surgical simulation. Medicine Meets Virtual Reality, 69–74.

Cormack, R.A., Tempany, C.M., et al., 2000. Optimizing target coverage by dosimetric feedback during prostate brachytherapy. International Journal of Radiation Oncology Biology and Physics 48 (4), 1245–1249.

Cosby, N., Leszczynski, K., 1998. Computer-aided radiation therapy simulation: image intensifier spatial distortion correction for large field of view digital flouroscopy. Physics in Medicine and Biology 43, 2265–2278.

Crouch, J., Schneider, C., 2005. A velocity dependent model for needle insertion in soft tissue. In: Proceedings of MICCAI. Springer-Verlag Berlin Heidelberg, Palm Springs, CA.

d'Aulignac, D., Balaniuk, R. et al., 2000. A haptic interface for a virtual exam of the human thigh. In: Proceedings of the IEEE International Conference on Robotics & Automation, pp. 2452–2456.

Davies, P.J., Carter, F.J., et al., 2002. Mathematical modeling for keyhole surgery simulations: a biomechanical model for spleen tissue. IMA Journal of Applied Mathematics 67, 41–67.

DiMaio, S.P., Salcudean, S. 2002. Needle insertion modeling and simulation. In: Proceedings of the IEEE International Conference on Robotics and Automation.

Fahrig, R., Moreau, M., et al., 1997. Three-dimensional computed tomographic reconstruction using a C-arm mounted XRII: correction of image intensifier distortion. Medical Physics 24 (7), 1097–1106.

Forest, C., Delingette, H. et al., 2002. Cutting simulation of manifold volumetric meshes. In: Proceedings of the Fifth International Conference on Medical Image Computing and Computer Assisted Intervention, vol. 2, pp. 235–244.

Gobbetti, E., 2000. Catheter insertion simulation with co-registered direct volume rendering and haptic feedback. Medicine Meets Virtual Reality, 96–98.

Gorman, P., 2000. A prototype haptic lumbar puncture simulator. In: Proceedings of Medicine Meets Virtual Reality, pp. 106–109.

Hendee, W., Ritenour, E., 2002. Fluoroscopy. Medical Imaging Physics. Wiley.

Heverly, M., Dupont, P., et al. 2005. Trajectory optimization for dynamic needle insertion. In: Proceedings of the IEEE International Conference on Robotics and Automation, Barcelona, Spain.

Hiemenz, L., 1996. A physiologically valid simulator for training residents to perform an epidural block. In: Proceedings of the IEEE Biomedical Engineering Conference, pp. 170–173.

Hong, J., Dohi, T., et al., 2004. An Ultrasound-driven needle-insertion robot for percutaneous cholecystomy. Physics in Medicine and Biology 49, 441–455.

Kataoka, H., Washio, T., et al. 2002. Measurement of tip and friction force acting on a needle during penetration. In: Proceedings of the Fifth International Conference on Medical Image Computing and Computer Assisted Intervention, pp. 216–223.

Kennedy, C.W., Hu, T., et al. 2002. Combining haptic and visual servoing for cardiothoracic procedures. In: Proceedings of the IEEE International Conference on Robotics and Automation, Washington, DC.

Kennedy, C.W., Hu, T., et al., 2002. A novel approach to robotic cardiac surgery using haptics and vision. Cardiovascular Engineering: An International Journal, 2002.

Kerdok, A.E., Cotin, S.M., et al., 2003. Truth cube: establishing physical standards for real time soft tissue simulation. Medical Image Analysis 7, 283–291.

Magill, J., Anderson, B., et al., 2004. Multi-axis mechanical simulator for epidural needle insertion. International Symposium on Medical Simulation.

Nienhuys, H., van der Stappen, F., 2003. Interactive needle insertions in 3D nonlinear material.

O'Leary, M.D., Simone, C., et al. 2003. robotic needle insertion: effects of friction and needle geometry. In: Proceedings of the IEEE International Conference on Robotics and Automation.

Ottensmeyer, M.P., Salisbury, J.K., 2001. In vivo data acquisition instrument for solid organ mechanical property measurement. In: Proceedings of the Fourth International Conference on Medical Image Computing and Computer-assisted Intervention.

Picinbono, G., Delingette, H., et al., 2001. Nonlinear and anisotropic elastic soft tissue models for medical simulation. In: Proceedings of the IEEE International Conference on Robotics and Automation.

Rudin, S., Bednarek, D.R., et al., 1991. Accurate characterization of image intensifier distortion. Medical Physics 18 (6), 1145–1151.

Simone, C., 2002. Modeling of Needle Insertion Forces for Percutaneous Therapies. Department of Mechanical Engineering. Baltimore, MD, The Johns Hopkins University.

Smith, W.L., Surry, K., et al., 2001. Three dimensional ultrasound-guided core needle breast biopsy. Ultrasound in Medicine and Biology 27 (8), 1025–1034.

Stoianovici, D., Whitcomb, L., et al., 1998. A modular surgical robotic system for image guided percutaneous procedures. In: Proceedings of the MICCAI.

Tholey, G., Desai, J.P., 2005. A general purpose 7 DOF haptic interface. In: Proceedings of the First Joint Eurohaptics Conference and Symposium on Haptic Interfaces for Virtual Environment and Teleoperator Systems, Pisa, Italy.

Vicini, F.A., Kini, V.R., et al., 1999. A comprehensive review of prostate cancer brachytherapy: defining an optimal technique. International Journal of Radiation Oncology Biology and Physics 44 (3), 483–491.